A Hybrid Strategy for the Design and Optimization of Coaxial Magnetic Gears

machines

MDPI

Article

A Hybrid Strategy for the Design and Optimization of Coaxial Magnetic Gears

Xinyan Zhang [1,2], Renato Galluzzi [3,*] and Nicola Amati [1,2]

[1] Department of Mechanical and Aerospace Engineering, Politecnico di Torino, 10129 Turin, Italy; xinyan.zhang@polito.it (X.Z.); nicola.amati@polito.it (N.A.)
[2] Center of Automotive Research and Sustainable Mobility, Politecnico di Torino, 10129 Turin, Italy
[3] School of Engineering and Sciences, Tecnologico de Monterrey, Mexico City 14380, Mexico
* Correspondence: renato.galluzzi@tec.mx

Abstract

Magnetic gear transmissions are promising alternatives to mechanical ones due to their contactless power transfer, reduced acoustic noise and vibration, inherent overload protection, and improved reliability. However, their design requires fast but accurate tools. While three-dimensional finite-element models offer good accuracy, their complexity hinders their use for design purposes. Two-dimensional representations, on the other hand, tend to overestimate performance due to the lack of end effects in the axial direction. This paper proposes a hybrid design and optimization framework for coaxial magnetic gears that couples a two-dimensional optimizer based on a genetic algorithm with a three-dimensional parametric model. The former model helps identify promising combinations in the design variable space. Then, specific selections are refined through the three-dimensional model. Numerical results show that both approaches exhibit consistent parameter trends, with a resulting prototype yielding a torque density of 213 Nm/L in an envelope contained within 90 mm of diameter and 16.57 mm of active length.

Keywords: coaxial magnetic gear; finite-element analysis; optimization; torque density; power losses; efficiency; torque ripple; end effects

Academic Editor: Wenjun (Chris) Zhang

Received: 14 November 2025
Revised: 6 December 2025
Accepted: 15 December 2025
Published: 18 December 2025

Citation: Zhang, X., Galluzzi, R., Amati, N. A Hybrid Strategy for the Design and Optimization of Coaxial Magnetic Gears. *Machines* **2026**, *13*, 1152. https://doi.org/10.3390/machines13121152

1. Introduction

Rotary transmission systems are fundamental in many industrial and vehicular applications, as they adapt the working point in terms of torque and angular speed of two or more rotating machines. While most of the transmission systems are geared mechanically, magnetic gears have emerged as promising alternatives to conventional ones. Magnetic transmissions exploit the contactless interaction between magnetic fields to transfer torque [1]. Furthermore, they inherently offer other advantages like reduced acoustic noise and vibration, reduced wear, and intrinsic overload protection [2]. These features make magnetic gears attractive in applications where reliability and efficiency are critical, including wind energy systems, electric vehicles, and actuators [3]. Among the various magnetic gear topologies, the coaxial magnetic gear (CMG) is particularly appealing due to its compactness [4], high torque density, and suitability for integration with electrical machines [5].

Despite these advantages, the practical deployment of CMGs remains limited, primarily due to challenges in their design and performance prediction [6,7]. Finite element analysis (FEA) has become the standard approach for evaluating magnetic gear characteristics [8]. While three-dimensional (3D) FEA provides the most accurate predictions by

accounting for leakage flux and axial end effects, it is computationally demanding and unsuitable for multiple parametric sweeps or optimization studies. On the other hand, two-dimensional (2D) FEA is computationally efficient but tends to overestimate torque capability, as it neglects axial end effects [9]. The literature confirms that these phenomena play a significant role in CMGs, especially due to the relatively short active length of these devices [3,10]. Consequently, there is a compromise between fast but simplified models and accurate but computationally expensive simulations, which hinders the design and optimization of CMGs. To overcome this trade-off, several strategies have been proposed in the literature. Analytical and lumped magnetic equivalent circuit models have been proposed to offer rapid evaluation and design intuition [11], but the linear material assumption can underestimate saturation effects and loss mechanisms [12]. Analytical models offer much faster computation times than FEA at the cost of losing accuracy and modeling flexibility [13]. These methods improve design robustness, but their implementation often requires careful calibration between models.

This study proposes a hybrid design and optimization framework for CMGs. It combines an initial optimization step based on genetic algorithms and 2D FEA. Subsequently, 3D FEA models are exploited to refine the design, considering end effects. The method is applied to a speed multiplier for vehicle chassis actuators.

The sequel of this work is organized as follows. Section 2 outlines the working principle of the studied solution. Then, Section 3 presents the design methodology. Section 4 applies the methodology to a particular case study and discusses the results in terms of average transmitted torque, torque ripple, unbalance forces, and efficiency, comparing these outcomes between 3D and 2D models. Finally, Section 5 concludes the work.

2. Operating Principle and Topology Selection

High torque density and intrinsic overload protection make magnetic gears suitable for their use in multiple applications, such as automotive actuators [14], wind turbines [15], and aircraft propulsion [16]. Moreover, the magnetic gear's contactless torque transmission yields favorable performance in acoustic noise when compared against traditional mechanical gears [7].

In this paper, a coaxial magnetic gear (CMG) with surface-mounted permanent magnets (PMs) is investigated as a replacement for the conventional mechanical gearbox in an automotive chassis actuator [17], aiming to achieve contactless torque transmission, reduced noise, and enhanced energy efficiency. The magnetic gear setup is shown in Figure 1a; it is divided into three components: (i) an inner rotor with N_i pole pairs and angular speed ω_i, which serves as the high-speed shaft; (ii) an outer rotor with N_o pole pairs and angular speed ω_o, used as the low-speed shaft; and (iii) an intermediate ferromagnetic modulator stage (cage rotor) with N_m pole pieces. Figure 1b,c show the geometric parameters used in this study, t_pmi and t_pmo represent the permanent-magnet (PM) thickness in the inner and outer rotor, respectively; t_bi and t_bo are the inner and outer back-iron thickness; t_m is the modulator thickness; t_g is the thickness of each of the two air gaps; the outer rotor radius is R_o; θ_i and θ_o are the angular spans of the inner and outer PMs; $\theta = 2\,\theta_\mathrm{m}$, with θ_m being the modulator angular span. S_i and S_o denote the number of segments per pole for inner and outer rotors. The parameters shown in Table 1 can be selected in a preliminary phase [18]. Hence, they remain unchanged during the 2D optimization and 3D validation in the following sections.

The CMG offers multiple operating modes depending on which member is fixed. When the modulators are fixed, the transmission ratio G_r is given by [11]

$$G_\mathrm{r} = \frac{\omega_\mathrm{i}}{\omega_\mathrm{o}} = -\frac{N_\mathrm{o}}{N_\mathrm{i}} \tag{1}$$

where the minus sign indicates that the inner and outer rotors rotate in opposite directions. The inner and outer rotors operate as the low-speed and high-speed rotors, respectively, and the absolute transmission ratio is $|G_r| = N_o/N_i = 14/3 \approx 4.667$. Furthermore, the number of pole pieces on the modulation stage should be [19]

$$N_m = N_i + N_o \tag{2}$$

In this work, modulators are selected as the stationary member, as this configuration enables a more compact and mechanically robust integration into an automotive chassis actuator. The objective of this study is not to identify globally optimal pole combinations but to evaluate geometric optimization trends under a fixed harmonic mode.

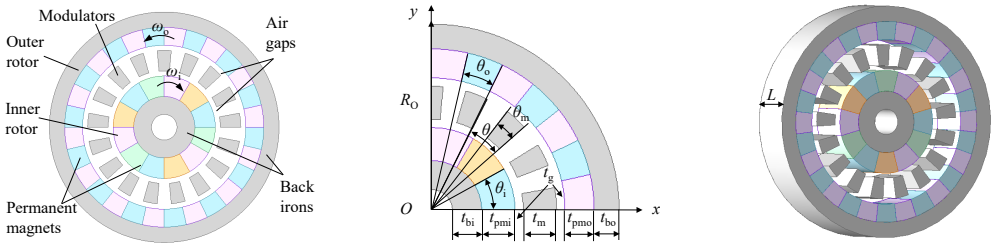

(**a**) (**b**) (**c**)

Figure 1. Coaxial magnetic gear (CMG) (**a**) cross-section view and (**b**) geometric parameter definitions in 2D and (**c**) 3D axial view.

Table 1. Fixed geometric parameters of the proposed magnetic gear.

Symbol	Description	Value	Unit
N_i	Inner rotor pole pairs	3	–
θ_i	Inner rotor angular span	$180/(S_i N_i)$	deg
N_m	Modulator pole pieces	17	–
θ_m	Modulator angular span	$180/N_m$	deg
R_o	Outer rotor outer radius	45	mm
N_o	Outer rotor pole pairs	14	–
θ_o	Outer rotor angular span	$180/(S_o N_o)$	deg
t_g	Air-gap thickness	0.5	mm
S_i	Inner rotor number of segments per pole	1 or 2	–
S_o	Outer rotor number of segments per pole	1 or 2	–

The instantaneous power balance of the magnetic gear stage can be expressed as

$$T_i\omega_i = T_o\omega_o + P_{loss} \tag{3}$$

where T_i, T_o, and T_m are the torques experienced by the inner rotor, outer rotor, and modulators, respectively. ω_i and ω_o are the inner and outer rotor speeds, respectively. The modulators are stationary, therefore, they do not contribute to mechanical power. P_{loss} represents the total power loss of the system.

The volumetric torque density (VTD) is defined in this work as a volume-based performance index, following a commonly adopted definition in the magnetic gear literature [7,20–22].

$$\text{VTD} = \frac{T_{o,max}}{\pi {R_o}^2 L} \tag{4}$$

where $T_{o,max}$ is the maximum torque, L is the axial stack length, and R_o is the outer rotor radius.

This definition of VTD follows common practice in literature and represents the torque normalized by the total cylindrical envelope volume of the magnetic gear. It should be noted that electromagnetic torque is physically produced by shear stresses. The present definition represents a global packaging-level torque density and may overestimate the local shear-based torque density, which depends on the effective radius.

One of the most important measures of a magnetic gear's performance is its stall torque, also denoted as maximum or pull-out torque. Pole slipping between the rotors results from the magnetic coupling's inability to sustain synchronous functioning when the applied load goes beyond this limit [23]. This phenomenon emphasizes how crucial it is to assess the torque limit in the design phase to guarantee functionality under known loads.

With the selected dimensions and parameters for the coaxial radial flux magnetic gear model, 2D finite-element simulations are set up in Ansoft Maxwell 2025R1. The starting point of the simulation was obtained from the unloaded (no-external-torque) condition, which is used solely to initialize the solution. Then, the stall torque is calculated as a function of mechanical angle when only the inner rotor is rotating.

Four CMG topologies were evaluated under identical geometric and material constraints, as shown in Figure 2. Figure 2a illustrates a topology with Halbach PM arrays on both rotors, with two segments per pole ($S_i = 2$, $S_o = 2$); Figure 2b uses a Halbach array only for the inner rotor, with two segments per pole on inner rotor and one segment per pole on outer rotor ($S_i = 2$, $S_o = 1$); Figure 2c exhibits pure radial magnetization on both rotors i.e., one segment per pole both rotors ($S_i = 1$, $S_o = 1$); Figure 2c exploits tangential magnetization on both rotors, with one segment per pole in both cases ($S_i = 1$, $S_o = 1$). The torque angle curves and volumetric torque densities are shown in Figure 3. It can be seen that the Halbach array delivers the highest torque performance, with a torque density of 181.36 Nm/L, followed by the Habach array on the inner rotor, with a torque density of 143.39 Nm/L. Despite its advantage in VTD, the Halbach array both rotors requires a significantly large number of small PM pieces on the outer rotor. Its practical implementation is hindered by the high part count and tight assembly tolerances, more complex magnetization, increased risk of chipping, rotor unbalance at speed, and higher cost [19]. The Halbach array on only the inner rotor offers a more favorable trade-off, as it retains a competitive torque waveform and VTD while substantially simplifying the rotor build and improving robustness. Therefore, the Halbach array on the inner rotor is selected for subsequent optimization and 3D validation. The other two types have significantly lower torque densities and are therefore not considered.

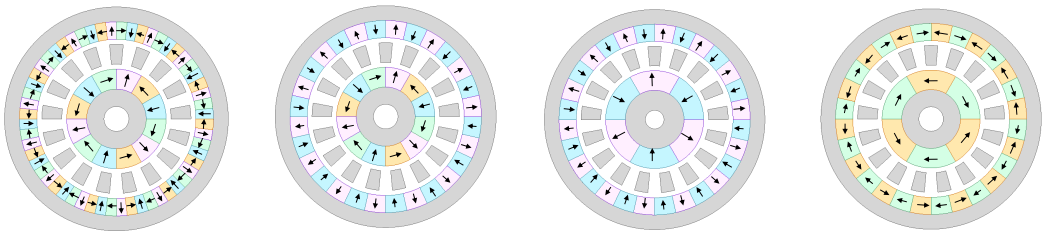

(**a**) (**b**) (**c**) (**d**)

Figure 2. Coaxial magnetic gear with different topologies (**a**) Halbach array on both rotors, (**b**) Halbach array on inner rotor (proposed), (**c**) radial magnetization on both rotors, and (**d**) tangential magnetization on both rotors.

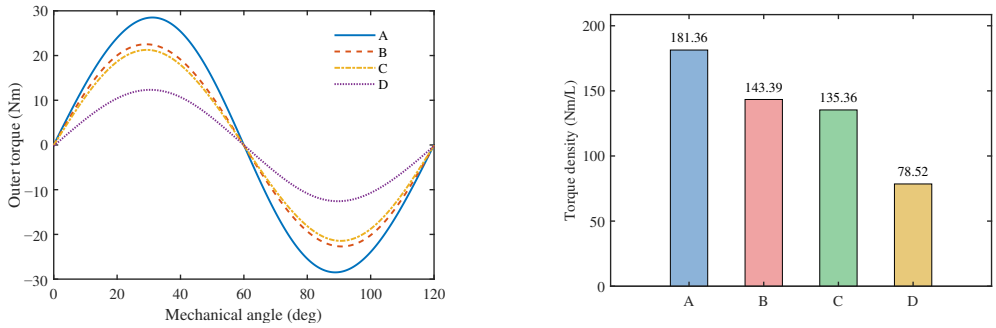

(**a**) (**b**)

Figure 3. Comparison of different topologies, case A is the Halbach array on both rotors, case B represents Halbach array only on the inner rotor, case C and case D are radial and tangential magnetization on both rotors, respectively (**a**) stall torque (maximum torque) and (**b**) volumetric torque density.

3. Design Method

3.1. Finite Element Modeling

FEA has been widely used for magnetic transmissions since the early works of the 90s [24] and remains the standard tool for accurate nonlinear evaluation. This study proposes full coaxial magnetic gear models that solve the magnetoquasistatic Maxwell equations using the **A**–ϕ formulation with nonlinear materials [25]. 2D and 3D models are built in cylindrical coordinates; the outer boundary is magnetically insulated, and periodicity is applied where appropriate. Nonlinear *B*-*H* properties are assigned to steel domains; the inner back iron is solid, while the modulators and outer back irons employ homogenized laminations (0.35 mm) [26]. Demagnetization effects are inherently captured by the solver when the local magnetic field approaches or exceeds the intrinsic coercivity. PMs are grade N50 NdFeB, consistent with prior magnetic gear prototypes that included this material for high torque density [27]. Kinematics are set to follow the absolute transmission ratio, $|G_r| = 4.667$ calculated with Equation (1), through sliding bands in 2D, and rotating subdomains in 3D [28]. Domains are meshed with quadratic elements with local refinement in the air gaps, at PM edges, and near modulator tips. Solutions are computed in the time domain to identify the dominant electrical harmonics. Torque is computed using the Maxwell stress tensor and losses are calculated from the field solution [29]. Both 2D and 3D models are built in cylindrical coordinates to match the coaxial geometry. The computational domain is truncated with magnetic insulation at the outer boundary, while periodicity is imposed where appropriate.

In this study, the second-order elements with targeted mesh refinement were employed. In the 2D model, the refinement is concentrated along the air gap boundaries and at the permanent-magnet–air interfaces to ensure accurate torque prediction. In the 3D model, additional refinement is introduced at the PM edges, the modulator surfaces, and across the full axial extent of the air gap, where flux fringing and end effects significantly influence torque ripple and eddy current loss. This mesh strategy guarantees consistent accuracy in resolving the torque transmission and loss evaluation.

3.2. Losses and Efficiency

The Bertotti iron loss separation model was used to calculate the iron loss, P_{iron}, which can be divided into three parts: hysteresis loss, eddy currents, and excess [29,30].

$$P_{\text{iron}} = \sum_{r \in \mathcal{S}} V_r \sum_{\nu \geq 1} \left[k_{\text{h}} (\nu f_{\text{e}}) \, |B_{r,\nu}|^{\alpha} + k_{\text{c}} (\nu f_{\text{e}})^2 \, |B_{r,\nu}|^2 + k_{\text{ex}} (\nu f_{\text{e}})^{1.5} \, |B_{r,\nu}|^{1.5} \right] \tag{5}$$

where $\mathcal{S}$ collects the steel regions (e.g., inner and outer back irons and modulators), V_r is the volume of the region, r, $B_{r,\nu}$ is the magnitude of the νth harmonic of the local flux density, f_{e} is the fundamental electrical frequency, and $k_{\text{h}}, k_{\text{c}}, k_{\text{ex}}, \alpha$ are material coefficients.

The excess losses are typically a minor component of the overall iron loss [31]. Therefore, they are neglected in this study. Permanent magnets (PMs) eddy current loss is computed via the time domain $J \cdot E$ (equivalently J^2/σ) volume integral [32]. Conversely, a hybrid approach to evaluate eddy current losses in PMs [33] is exploited. An equivalent current sheet is first obtained from a 2D analytical model, which is then applied in a 3D FEA to capture end effects. The eddy current loss in PMs over one electrical period τ_{e} is

$$P_{\text{PM}} = \frac{1}{\tau_{\text{e}}} \int_0^{\tau_{\text{e}}} \int_{V_{\text{PM}}} p_{\text{PM}} \, \mathrm{d}V \, \mathrm{d}t = \frac{1}{\tau_{\text{e}}} \int_0^{\tau_{\text{e}}} \int_{V_{\text{PM}}} \frac{J^2}{\sigma} \, \mathrm{d}V \, \mathrm{d}t \tag{6}$$

where V_{PM} is the PMs volume, τ_{e} is the electrical period, J is the eddy current density (A/m^2), σ is the electrical conductivity of the PM (S/m), and $p_{\text{PM}} = J^2/\sigma$ is the instantaneous volumetric eddy current loss density (W/m^3).

As illustrated in Figure 4, component-wise electromagnetic loss distributions under two scenarios: Figure 4a shows the variation of total and distributed losses with speed for a torque-angle of 30° (maximum torque), and Figure 4b shows the variation of losses with transmitted inner torque at a constant inner rotor speed of 6000 r/min. Each color region denotes the contribution of the outer PMs, inner PMs, outer back iron, modulators, and inner back iron.The CMG total losses increase rapidly with the inner rotor speed and decrease smoothly with the inner rotor torque. The modulators and outer back iron emerge as the dominant contributors. This behavior is consistent with core loss physics: electromagnetic losses scale strongly with electrical frequency and with local flux density harmonics, so iron regions experiencing large alternating flux near the modulator tips and back iron dominate [34]. Although the Halbach configuration reduces the radial leakage inside PMs, it does not eliminate the tangential harmonic components introduced by modulation. These alternating components penetrate the PMs and increase with rotational speed, meaning that PM eddy-current losses can become non-negligible under high-speed operation, even if they remain lower than the iron losses at moderate speeds. Since eddy-current losses scale approximately with the square of the electrical frequency, their increase at high speed is particularly pronounced. Consequently, to obtained improved performance in CMGs, the design should primarily focus on reducing the dominant iron losses through geometric optimization or the use of low-loss laminated materials, while also accounting for potential PM losses in high-speed applications.

The efficiency of the CMG is calculated by using the torque, iron losses and PM losses, following the expression adapted from [35]. Other types of losses are neglected.

$$\eta = \frac{T_{\text{o}} \omega_{\text{o}}}{T_{\text{o}} \omega_{\text{o}} + P_{\text{loss}}} \tag{7}$$

$$P_{\text{loss}} = P_{\text{iron}} + P_{\text{PM}} \tag{8}$$

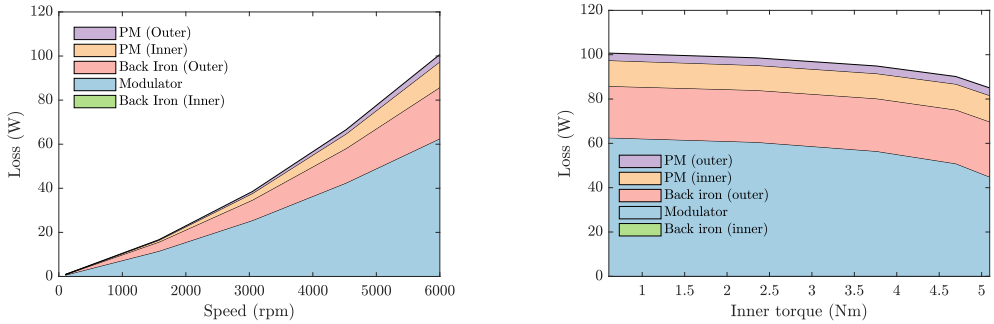

(**a**) (**b**)

Figure 4. Component-wise loss distributions of the proposed magnetic gear under different operating conditions (**a**) electromagnetic loss versus rotational speed and (**b**) electromagnetic loss versus transmitted inner torque.

3.3. Hybrid Stochastic Optimization

In this section, we present a hybrid stochastic optimization method used to maximize the torque transmission capability of the CMG. Hybrid stochastic optimization may provide, in principle, a satisfactory compromise between computational effort and accuracy in estimating torque performance, making it suitable for magnetic gear design. To this end, a combination of 2D FEA, GA, and 3D parametric model is employed. In this hybrid strategy, the 2D FEA is fast and suitable for GA-based global space search, while 3D FEA is accurate and captures the essential end effects. This strategy is computationally efficient for exploration and physically reliable for final validation, ensuring both speed and accuracy in optimizing the CMG torque performance.

In this work, several pilot convergence tests were performed before the final optimization. The population size of 100, 35 generations, crossover probability of 0.7, and mutation probability of 0.1 were selected in magnetic gear optimization. Parameter ranges of this order have been reported in [5,8,28] as providing a good balance between exploration and computational cost. Increasing the population to 150 or decreasing it to 50 did not improve the solution quality, while significantly affecting computation time. Similarly, crossover probabilities in the range 0.6–0.8 and mutation probabilities of 0.05–0.15 exhibited comparable convergence trends. The chosen configuration therefore represents a robust and computationally efficient setting rather than an attempt to fine-tune GA hyperparameters.

The proposed CMG with a hybrid Halbach array (only inner rotor) involves many coupled design variables. With the proposed topology fixed parameters in Table 1, we employed a genetic algorithm in MATLAB coupled with a 2D finite-element model in Finite Element Method Magnetics (FEMM) to maximize the VTD [36]. The search enforced the radial envelope constraint

$$t_{\mathrm{pmi}} + t_{\mathrm{m}} + t_{\mathrm{pmo}} + t_{\mathrm{bi}} + t_{\mathrm{bo}} + 2t_{\mathrm{g}} \leq R_{\mathrm{o}} \tag{9}$$

initialized from the bounds $t_{\mathrm{pmi}}, t_{\mathrm{pmo}} \in [5, 15]$ mm, $t_{\mathrm{m}}, t_{\mathrm{bi}}, t_{\mathrm{bo}} \in [5, 10]$ mm, and $L \in [10, 20]$ mm.

The full optimization population over the design space is shown in Figure 5. It can be seen how the volumetric torque density varies with structural parameters, revealing strong positive correlations between VTD and the optimized parameters, especially for the inner magnet thickness.

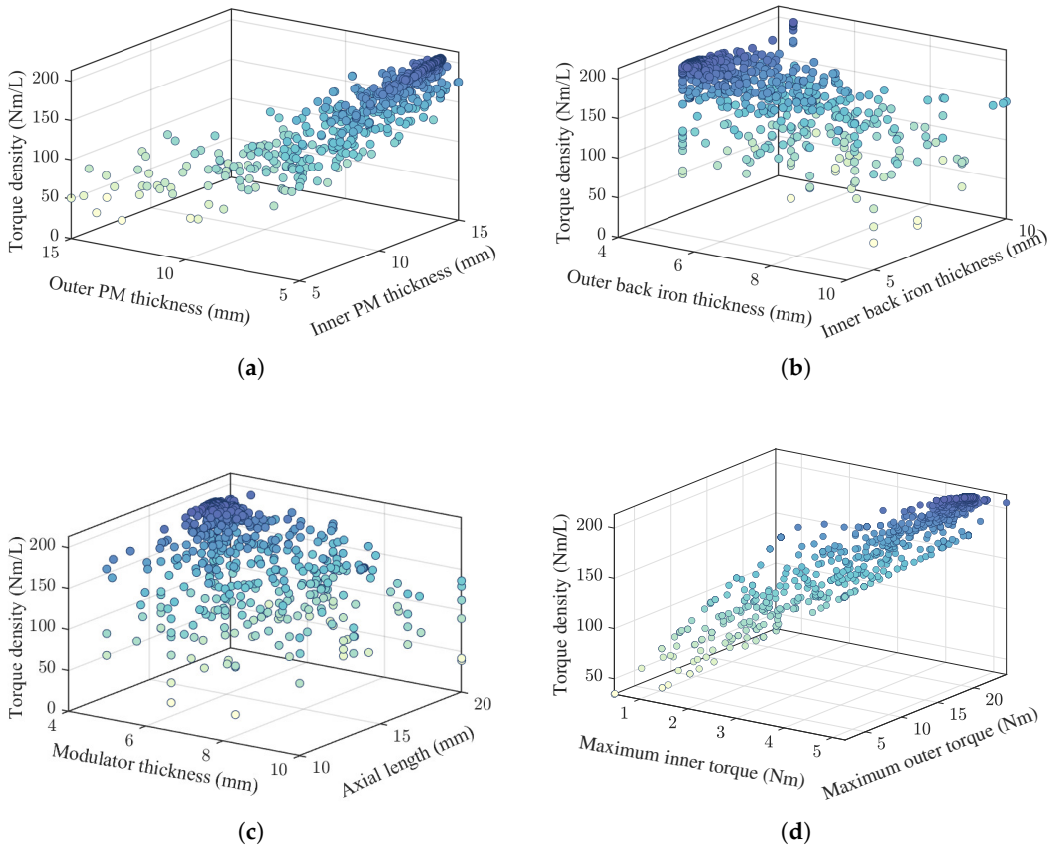

Figure 5. Distribution of the optimization population in the design space (**a**) PM thicknesses (**b**) back-iron thicknesses (**c**) modulator thickness and axial length (**d**) maximum torques (stall torques).

For computational efficiency, a screening sensitivity analysis precedes the GA to fix low-influence variables. Subsequently, the GA queries the fast model for evolution while optimal designs are checked with 3D FEA to account for end effects. This analysis reveals how individual variables influence the CMG's electromagnetic performance. Parameters with the largest impact are retained for optimization, while low-influence variables are fixed to nominal values, thereby shrinking the search space, shortening calculation time, and improving optimization efficiency.

To quantify the influence of each design variable on the objective, the Pearson correlation coefficient [37] is employed. For a design variable, x_i, and the objective, y, the Pearson coefficient is defined as

$$\lambda(x_i, y) = \frac{\mathrm{cov}(x_i, y)}{\sigma_{x_i}\,\sigma_y} \tag{10}$$

where σ_{x_i} and σ_y are the standard deviations of x_i and y, respectively. A positive value indicates that increasing x_i tends to increase the objective, whereas a negative value indicates the opposite trend. To indicate direction (beneficial vs. detrimental performance), the sign of the bars in the plots is taken from the correlation while the bar height reflects the magnitude. Larger values denote stronger influence. In Figure 6a, the inner PM thickness, t_{pmi}, is most beneficial ($\sim$+0.87); the outer PM thickness, t_{pmo}, and the modulator thickness, t_{m}, are strongly detrimental (~ -0.83 and -0.77); the back irons, t_{bi}, t_{bo}, are moderately detrimental ($\sim -0.61, -0.78$); and the stack length, L, is weakly positive ($\sim$+0.17). Figure 6b shows that the $(t_{\mathrm{pmi}}, t_{\mathrm{pmo}})$ contour reveals a high VTD ridge at larger t_{pmi} with smaller t_{pmo}, guiding the design toward higher t_{pmi}, lower t_{pmo}.

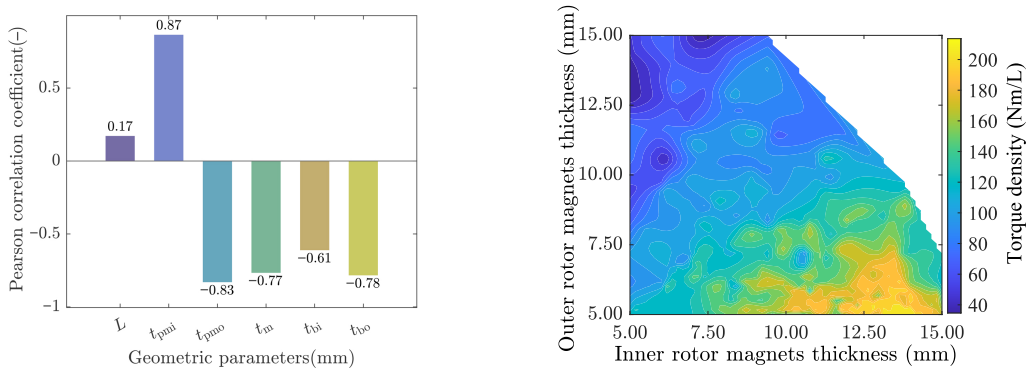

(**a**) (**b**)

Figure 6. Correlation and interaction analysis of geometric parameters affecting torque density and (**a**) correlation coefficients for torque density, where the sign indicates the direction of correlation (positive or negative), and a larger absolute value represents a stronger correlation and (**b**) torque density contour with respect to inner and outer PM thicknesses.

The refined search ranges and fixed inputs used for subsequent evaluation are summarized in Table 2.

Table 2. Optimization variables of the CMG after GA-based 2D FEA and refined 3D analysis.

Symbol	Description	2D Search Space	3D Refined Space	Unit
L	Axial stack length	[10, 20]	[14, 19]	mm
t_{pmi}	Inner rotor magnet thickness	[5, 15]	[12, 14.5]	mm
t_{pmo}	Outer rotor magnet thickness	[5, 15]	[5, 7]	mm
t_{m}	Modulator thickness	[5, 10]	[5, 7.5]	mm
t_{bi}	Inner rotor back-iron thickness	[5, 10]	6.5	mm
t_{bo}	Outer rotor back-iron thickness	[5, 10]	5	mm

3.4. Validation Plan and Metrics

Three components of axial end effects, leakage, fringing, and escaping have been reported [13], where leakage denotes flux bypassing the intended path, fringing refers to lateral flux spreading at magnetic discontinuities, and escaping describes flux leaving the active region without re-entering the air gap. The last one is particularly important for CMG because the torque transmission depends on precise harmonic modulation across the modulators. Figure 7 shows the magnetic flux density distributions obtained from the 2D and 3D FEA models of the proposed magnetic gear. Figure 7a shows the idealized steady-state flux pattern in 2D FEA, where end effects are neglected and the magnetic field is evenly distributed along the axial direction. In contrast, the 3D FEA results in the influence of axial flux leakage and non-uniform field distribution caused by the axial length. The half cross-section in Figure 7b visualizes the internal magnetic flux distribution, while the front view in Figure 7c confirms the periodic modulation of flux density. The cross section in Figure 7d shows the axial variation of the magnetic flux density, demonstrating that non-uniform axial flux patterns are inherently in the 3D model. In contrast, the 2D FEA relies on the assumption of axial uniformity, which cannot capture these features. This discrepancy in modeling is also a primary contributor to the differences in evaluation results between 2D and 3D FEA.

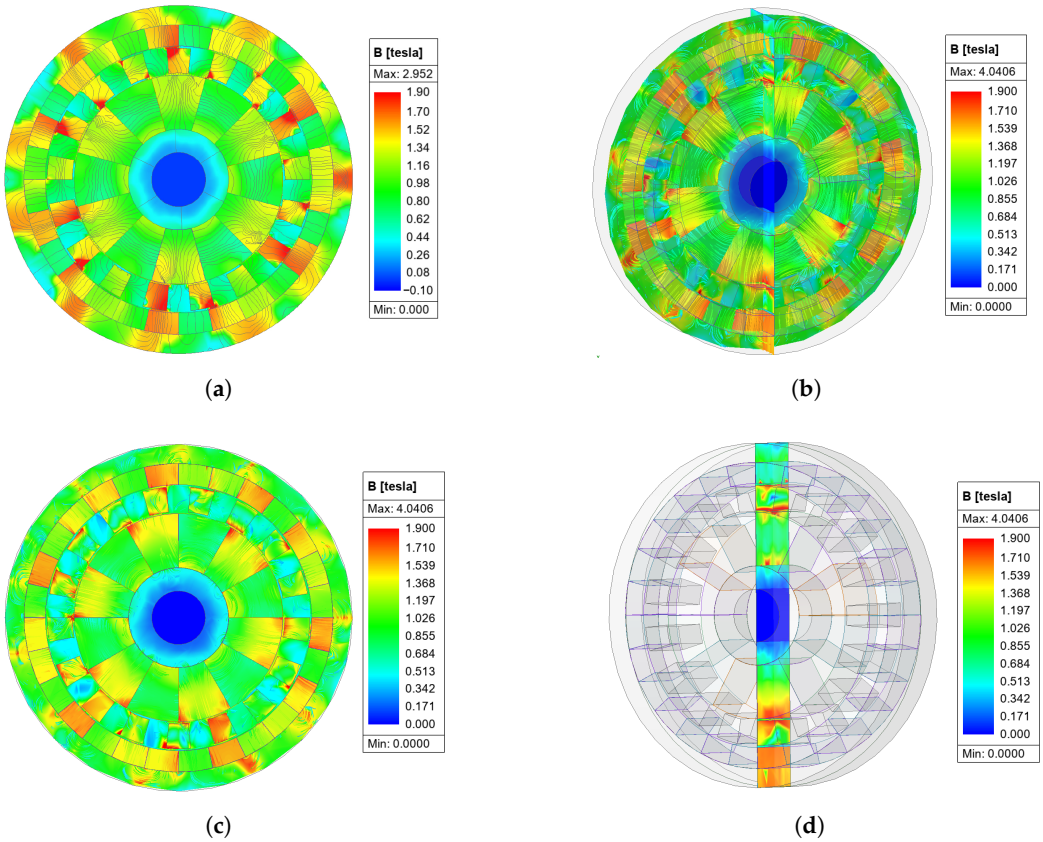

Figure 7. Comparison of magnetic flux density distributions between 2D and 3D FEA models (**a**) 2D FEA full cross section (**b**) magnetic field distribution of the magnetic gear obtained from 3D model, illustrated on the plane at half the axial length and half the radial span (**c**) radial cross-section front view (**d**) axial section view.

To quantify the extent of the correlation between 2D and 3D FEA results, the results obtained from the 2D FEM model are used as a reference approximation, whereas the 3D FEM results are regarded as the more accurate prediction. The 3D-2D ratios of torque, λ_T, and loss, λ_P, between the 2D evaluation and the 3D are defined as [9,13]

$$\lambda_T = \frac{T_{3D}}{T_{2D}} \tag{11}$$

$$\lambda_P = \frac{P_{3D}}{P_{2D}} \tag{12}$$

where T_{2D} and T_{3D} represent the predicted steady state electromagnetic stall torque from 2D and 3D FEA, respectively. Similarly, P_{2D} and P_{3D} are the corresponding losses (including core loss and eddy current loss) averaged over one electrical period.

Most 2D–3D discrepancies originate from axial end effects and the associated axial flux leakage. The 2D–3D deviation is not a constant offset but varies across the design space. Although space-mapping or surrogate corrections are possible, the parameter dependence of end effects makes a single global correction unreliable without extensive 3D sampling.

4. Results and Discussion

A first analysis was conducted to study the influence of several parameters on the stall torque and electromagnetic loss. For torque, we take the magnitude of the mean stall torque to avoid sign issues. The design was evaluated by 2D and 3D FEM with different CMG axial lengths. In the case of the axial length between $L = 5\,\text{mm}$ and $L = 65\,\text{mm}$, which

corresponds to an aspect ratio range between 0.056 to 0.722 ($a = L/2R_o$). All simulations by 2D and 3D FEA have significantly different stall torque and loss versus aspect ratio curves, as shown in Figure 8.

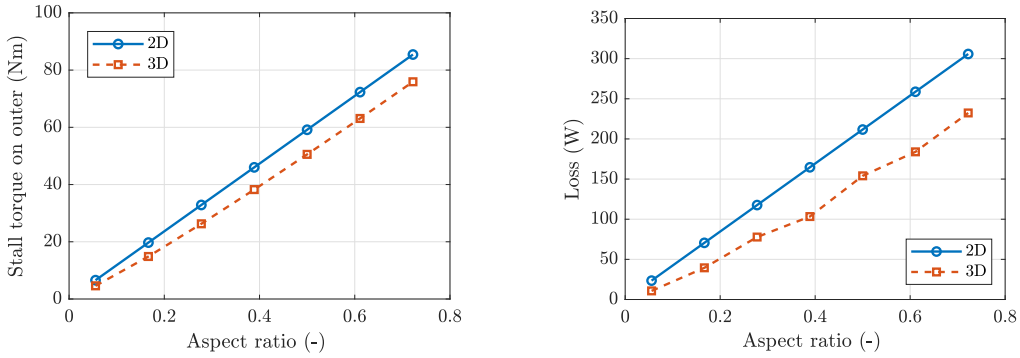

(**a**) (**b**)

Figure 8. (**a**) Stall torque (maximum torque) and (**b**) electromagnetic loss as functions of the aspect ratio.

Both the stall torque and the electromagnetic loss increase with aspect ratio, and become slightly sub-linear for short stacks due to end-region leakage and fringing. The 3D predictions remain below the 2D results because only the 3D model captures these end-region and three-dimensional effects.

The effect of the inner magnet thickness on the stall torque and loss is illustrated in Figures 9 and 10. In the simulated model, the outer magnet thickness and modulator thickness were kept constant. It can be seen that the 2D and 3D results follow similar trends, 3D predictions remaining slightly lower, because only the 3D FEA captures end-region and 3D effects. The torque and loss normalized by magnet thickness decrease as the magnet thickness increases; however, this trend mainly reflects the normalization and the diminishing incremental benefit of adding more magnet volume, rather than a fundamental loading limit. This observation is consistent with the diminishing-return behavior discussed in [13].

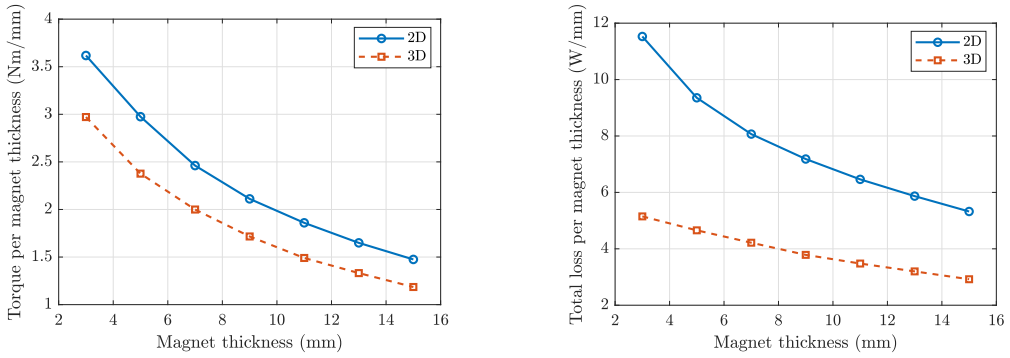

(**a**) (**b**)

Figure 9. (**a**) Stall torque (maximum torque) per PM thickness and (**b**) electromagnetic loss per PM thickness as functions of the PM thickness.

The impact of the axial length (stack length L) on the CMG with a hybrid Halbach array is shown in Figure 11a. An axial length $L = 16.57$ mm was selected from optimal resolutions, as this still guarantees a high VTD. The stall torque (maximum torque) increases with the stack length, L. Correspondingly, the volumetric torque density shows a small but measurable rise, because the torque grows slightly faster than the active volume as the relative influence of 3D fringing and edge effects diminishes with increasing axial length. Across the range, the 3D FEA predictions are systematically lower than the 2D results

because the 3D FEA captures effects that are absent in 2D, including axial end phenomena, three-dimensional fringing, edge saturation, and harmonic distortion, which have been reported in [7,25,38]. As a result, 2D FEA tends to overestimate the torque capability, whereas 3D FEA provides a more realistic prediction at the cost of higher computational effort.

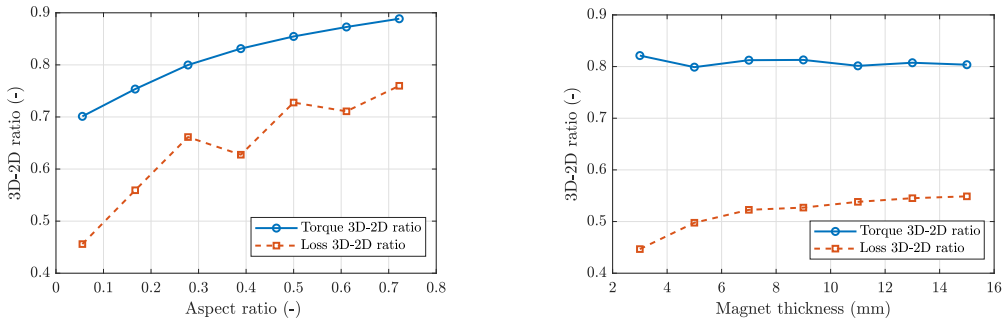

Figure 10. Comparison of 3D-2D ratios between 3D and 2D FEA (**a**) variation of torque and loss 3D-2D ratios and (**b**) variation of 3D-2D ratios with magnet thickness.

Wong et al. reported that reducing the axial length of the modulators, L_m, leads to an improvement in volumetric torque density, owing to increased flux concentration and altered harmonic coupling [18]. Accordingly, Figure 11b demonstrates the torque transmission at different lamination axial lengths,L_m, with the axial lengths of inner and outer rotors fixed at $L = 16.57$ mm. It can be seen that maximum torque and VTD occur when $L_m = 15.8$ mm. These yielded stall torque and VTD of 16.51 Nm and 161.88 Nm/L, with an improvement of 1.5 %. Thus, the value of L_m was decreased to 15.8 mm for the final design.

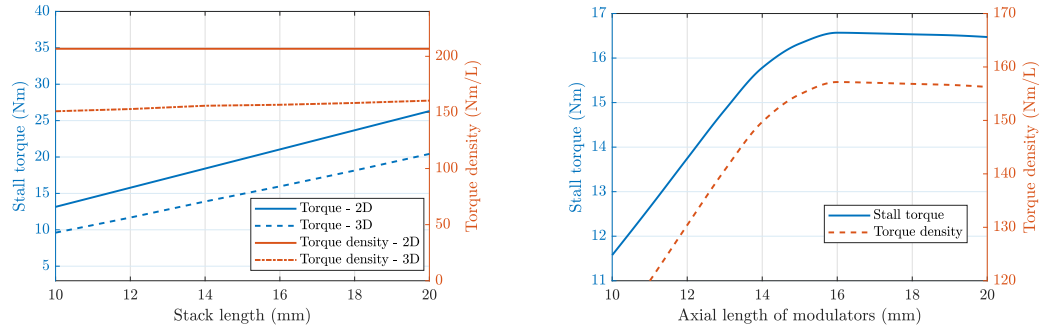

Figure 11. Stall torque (maximum torque) and volumetric torque density (VTD) comparison (**a**) influence of axial length and (**b**) influence of axial length of modulators 3D FEA.

4.1. Torque Transmission

In a magnetic gear, the torque is transmitted between the rotors through the magnetic coupling established by the modulators. The electromagnetic torque on each rotor fluctuates periodically with time, producing torque ripple due to the spatial harmonics in the air-gap flux. Prior work has already demonstrated the need to assess torque ripple and electromagnetic force harmonics in flux-modulated converters from a structural standpoint [25]. Additionally, higher losses can be attributed to increased bearing friction due to unbalanced forces [39]. However, the converter studied in literature differs from the present topology and assumes conventionally manufactured modulators. Here, we quantify the torque ripple and the radial and tangential forces (X, Y force components) for

our design. The torque ripple coefficient k_{rip} quantifies the relative torque variation over one steady-state period and is defined as

$$k_{\text{rip}} = \frac{T_{\max} - T_{\min}}{2T_{\text{avg}}} \tag{13}$$

where $T_{\max}$, $T_{\min}$, and T_{avg} are the maximum, minimum, and average electromagnetic torque, respectively.

The instantaneous torque responses of the inner and outer rotors (load angle of 30°, inner rotor speed of 6000 r/min) are illustrated in Figures 12 and 13. The transient simulation was carried out over a total duration of 400 ms with 2000 uniformly spaced sampling points, corresponding to a time step of 200 µs. It can be observed that the 3D FEA predicts a noticeably higher torque ripple compared with the 2D FEA. Specifically, the torque ripple coefficient of the inner rotor increases from 1.27% (2D FEA) to 6.83% (3D FEA), while the torque ripple of the outer rotor rises from 0.84% (2D FEA) to 1.67% (3D FEA). The higher torque ripple predicted in 3D arises from end effects, leakage flux, and additional 3D harmonic components, which are not captured in the 2D formulation. These axial variations in the air gaps increase the periodic torque fluctuation on the inner rotor.

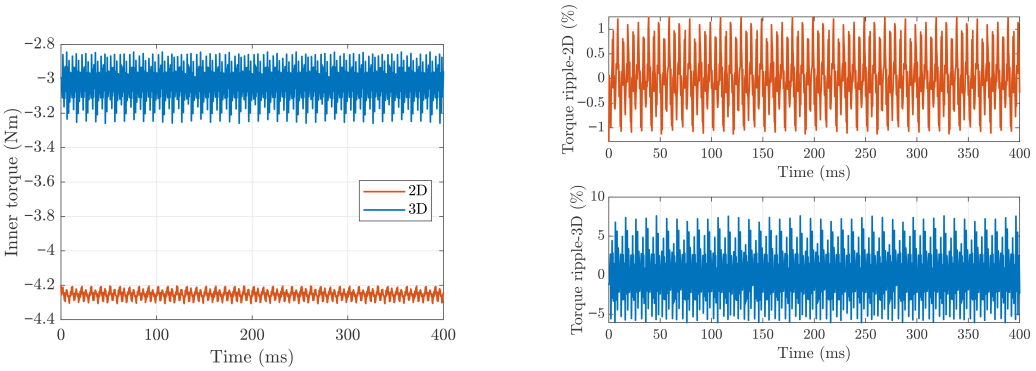

Figure 12. Comparison between 2D and 3D FEA inner torque (**a**) inner torque under steady-state operation and (**b**) inner torque ripple for 2D and 3D FEA.

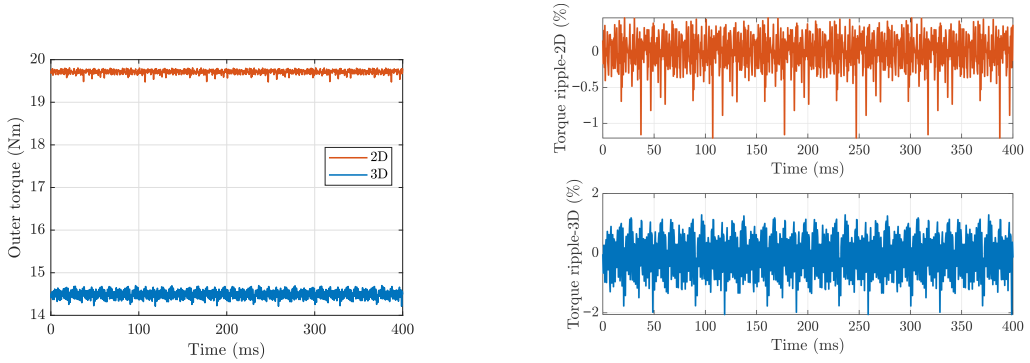

Figure 13. Comparison between 2D and 3D FEA outer torque (**a**) outer torque under steady-state operation and (**b**) outer torque ripple for 2D and 3D FEA.

4.2. Unbalance Force

In this subsection, the unbalance forces acting on the modulators (stator) are investigated. These forces can contribute to vibration, acoustic noise, and mechanical stress in practical applications [40], making them important design considerations. Both radial force, X component (F_x), and tangential force, Y component (F_y), exhibit significantly different

characteristics, as illustrated in Figure 14. The force in 3D shows larger fluctuation amplitudes and richer harmonic content, mainly due to the axial flux components and the end effect. In contrast, the smoother force in 2D tends to underestimate the magnitude of the force. These discrepancies are consistent with the torque ripple behavior observed earlier [25], indicating that the simplified 2D approximation neglects key spatial variations of the magnetic field.

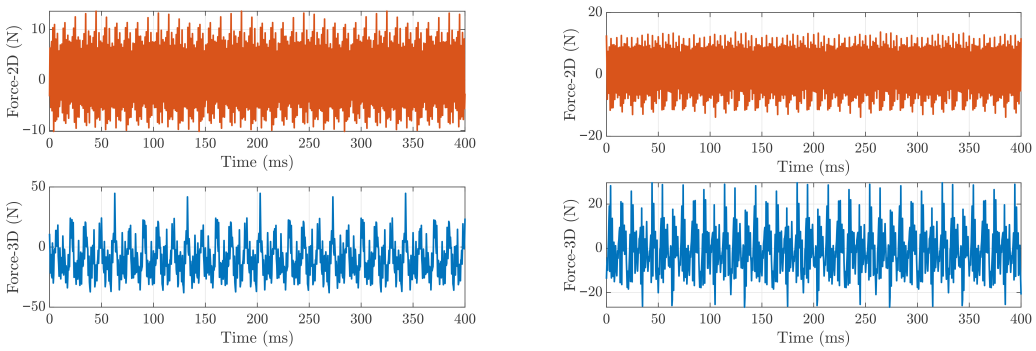

Figure 14. Comparison of electromagnetic force components between 2D and 3D FEA on the modulators (stator) (**a**) radial force, and (**b**) tangential force.

The relationship between unbalance electromagnetic forces and torque ripple is not universal, it depends on the CMG topology, the number of modulators, and harmonic interactions as reported in [22]. As reported in [38], an odd number of modulators inherently introduces radial unbalance force. However, our design still exhibits low torque ripple. This is mainly because the Halbach magnetization and the pole pair mismatch reduce the amplitude of the dominant torque ripple harmonics. Overall, the comparison results indicate that while 2D FEA provides a reasonable estimation of average torque, it underpredicts torque ripple and force harmonics. Therefore, 3D simulations are fundamental for accurate assessment of dynamic performance and mechanical reliability.

4.3. Efficiency Estimation

Magnetic gear losses are dominated by operating speed and vary only mildly with load torque, as shown in Figure 15a, consistent with prior observations [31]. A comparison of 2D and 3D FEA as Table 3 shows that the 2D model overestimates VTD by about 24% relative to the 3D model, which lies within the 20–40% overestimation range reported in the literature [39,41]. While absolute magnitudes differ, the operating point trends predicted by 2D and 3D are consistent (i.e., similar variation across speed and load angle), with small point-wise deviations when trends are compared. The operating points selected in this study are representative of typical CMG usage; however, they do not exhaustively cover all possible load angles or speed conditions.

Table 3. Comparison between 2D and 3D FEA results.

Description	$T_{i,max}$ (Nm)	$T_{o,max}$ (Nm)	VTD (Nm/L)	P_{loss} (W)	η (%)
2D FEA	4.60	21.76	213.31	98.76	96.88
3D FEA	3.49	16.51	161.88	84.43	96.92
Δ (3D–2D)/2D (%)	−24.09	−24.11	−24.11	−14.5	0.04

Figure 15b depicts total loss versus speed for multiple initial inner rotor angles (which correspond to different torque loading conditions). Both 2D and 3D results exhibit a comparable monotonic increase in loss with speed. However, their absolute values differ.

Notably, the 3D FEA predicts lower total loss than the 2D FEA, and the relative discrepancy in loss is larger than that for torque. This is because at the operating conditions, the axial flux spreading and the relatively large electromagnetic skin depth reduce the effective radial flux gradients within the PMs and back iron. In the 3D FEA, these axial leakage paths naturally soften the local $\partial B/\partial r$ distribution that drives eddy current formation. Conversely, the 2D FEA constrains the field to remain strictly uniform along the axial direction and forces all eddy current loops to close within the r-θ plane, thereby artificially strengthening the induced currents. As a result, the 2D FEA tends to overestimate both PMs and iron eddy losses, whereas the 3D FEA captures the attenuation of end region fields and the reduced eddy current circulation.

Such behavior has also been reported in several low-frequency, low aspect ratio PM devices [9,32,42–45], where 3D simulations exhibit lower losses than 2D due to weakened axial current paths and reduced flux concentration near magnet edges. This confirms that, in the frequency range and geometric regime relevant to this study, loss end effects are more dominant than torque end effects, leading to a larger 2D and 3D discrepancy in loss predictions.

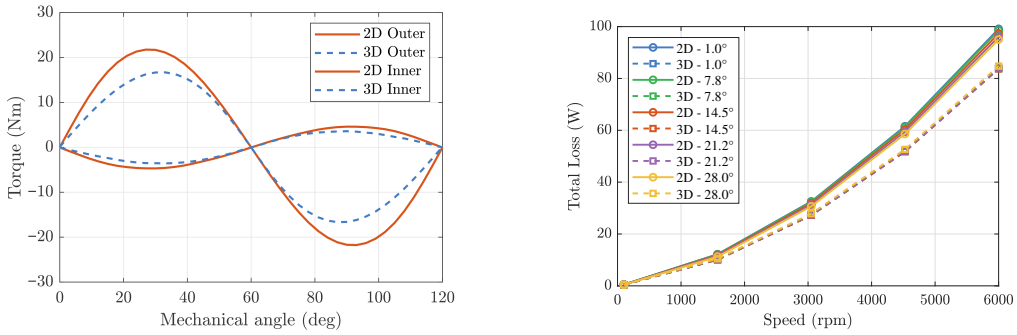

(**a**) (**b**)

Figure 15. Comparison between 2D and 3D FEA results (**a**) stall torque (maximum torque) and (**b**) total electromagnetic loss for different mechanical angles (2D: solid line, 3D: dashed line).

The efficiency maps in Figure 16 (with inner rotor speed from 100 r/min to 6000 r/min) further confirm a common trend in both models: efficiency increases with load torque, and losses scale primarily with speed, in agreement with [20,46].

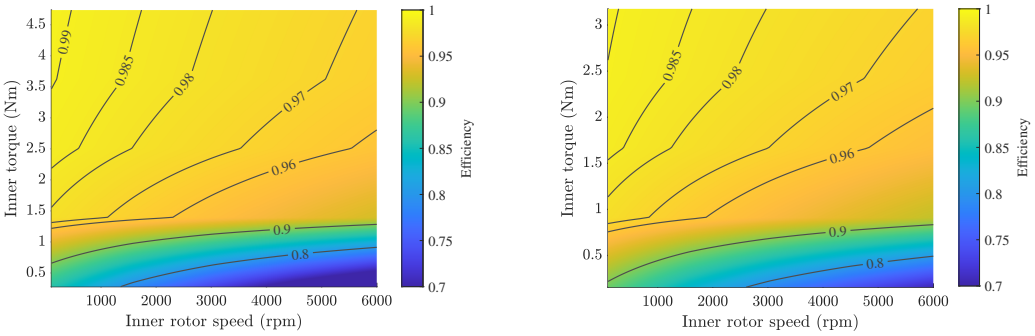

(**a**) (**b**)

Figure 16. Efficiency maps versus inner rotor speed and torque (**a**) 2D FEA results and (**b**) 3D FEA results.

Although an experimental prototype is not included in the present study, the accuracy of 3D FEA for coaxial magnetic gears has been widely reported in the literature. Experimental validations in [18,20,26] show that 3D simulations typically predict the transmitted torque within 8–15% of measurements, while 2D FEA tends to overestimate torque by

20–40% [39,41] due to the absence of axial end effects. Similarly, iron loss (core loss) and PM eddy current loss predictions generally exhibit 10–20% [31,33,47] deviation from experimental results, depending on lamination anisotropy and material properties. The 24% torque difference between the 2D and 3D predictions observed in this work therefore lies well within the range reported in prior CMG validation studies, indicating that the adopted 3D model exhibits representative physical accuracy.

After 3D verification (and minor rounding to catalog available dimensions), we selected the geometry that maximizes VTD while meeting loss and efficiency targets. The final design parameters of the proposed CMG are summarized in Table 4.

Table 4. Final design parameters of the CMG.

Symbol	Description	Value	Unit
R_o	Outer rotor radius	45	mm
L	Axial stack length of PM and back irons	16.57	mm
L_m	Axial stack length of modulators	15.8	mm
t_{pmi}	Inner rotor magnet thickness	13.8	mm
t_{pmo}	Outer rotor magnet thickness	5.5	mm
t_m	Modulator thickness	6.5	mm
t_{bi}	Inner rotor back-iron thickness	6	mm
t_{bo}	Outer rotor back-iron thickness	5.0	mm
t_g	Air-gap thickness	0.5	mm

4.4. Computation Time Comparison

To quantify the computational benefit of the proposed hybrid strategy, the evaluation times of the 2D and 3D FEA were benchmarked on a workstation equipped with an Intel® Core™ i9-185H processor (2.30 GHz, 14 cores) and 64 GB RAM.

A single 2D FEA torque–angle evaluation requires only 0.8–1.5 s, enabling rapid population-based optimization. In contrast, a transient 3D FEA simulation requires 35–55 min per design point. This corresponds to a slowdown of approximately 1200–2000× relative to 2D analysis. Comparable 2D–3D computation costs have been reported in the literature [35,48].

During optimization, the GA evaluates roughly 2500–3000 candidates. A 3D FEA search would therefore require several weeks of computation, whereas the proposed hybrid workflow completes the 2D optimization stage within 3–4 h and the 3D refinement within 10–15 h. Thus, the full optimization and validation process is completed within four working days. The computation time is summarized in Table 5.

Table 5. Computation time comparison of the proposed hybrid method.

Task	Time per Evaluation	Notes
2D FEA (torque–angle)	0.8–1.5 s	Used for GA exploration
3D FEA (transient)	35–55 min	Includes end effects and eddy currents
GA population size	—	2500–3000 evaluations
2D optimization stage	3–4 h	MATLAB–FEMM coupling
3D refinement stage	10–15 h	Detailed verification
Full hybrid cycle	4 working days	Optimization + validation

5. Conclusions

This paper established a hybrid strategy that integrates 2D FEA-based genetic algorithm optimization with 3D FEA-based parametric modeling, providing an effective framework for the design and optimization of coaxial magnetic gears. The main conclusions of this work are summarized as follows:

1. A two-level hybrid optimization framework combining fast 2D FEA-based GA optimization with high fidelity 3D FEA refinement was proposed to explore and accurately assess CMG designs efficiently.
2. Owing to its computational efficiency and its ability to capture the dominant geometric dependencies of torque and loss, 2D FEA was suitable for population evaluation and early-stage screening.
3. 3D FEA incorporated axial end effects that critically affect torque and loss predictions, particularly for short axial stack lengths where 2D models tend to overestimate performance.
4. The discrepancies between 2D and 3D FEA were governed by the combined influence of axial dimensions, magnet thickness, and modulation structure. These factors affected losses, torque, and ripple differently, making 3D evaluation essential for accurate performance assessment.
5. The optimized CMG achieved balanced performance in volumetric torque density, torque ripple, unbalanced force, and efficiency, demonstrating the effectiveness of the hybrid design workflow.

Future work will focus on prototype fabrication for experimental validation, extended thermal and loss modeling, and the investigation of alternative core materials and magnet grades considering torque density, efficiency, and cost.

Author Contributions: Conceptualization, R.G. and N.A.; methodology, X.Z. and R.G.; software, X.Z.; validation, X.Z. R.G.; formal analysis, R.G. and X.Z.; investigation, R.G. and X.Z.; resources, N.A.; data curation, R.G. and X.Z.; writing—original draft preparation, X.Z., R.G. and N.A.; writing—review and editing, R.G.; visualization, X.Z. and R.G.; supervision, R.G. and N.A.; project administration, N.A.; funding acquisition, N.A. All authors have read and agreed to the published version of the manuscript.

Funding: This research was partially funded by the European Commission under grant no. 101138110 (SmartCorners project) and supported by the Program of China Scholarship Council (Grant No. 202209510005).

Data Availability Statement: The original contributions presented in this study are included in the article. Further inquiries can be directed to the corresponding author.

Conflicts of Interest: The authors declare no conflicts of interest.

References

1. Atallah, K.; Howe, D. A novel high-performance magnetic gear. *IEEE Trans. Magn.* **2001**, *37*, 2844–2846. [CrossRef]
2. Seyedi, S.M.; Gardner, M.C.; Johnson, M.; Hasanpour, S.; Praslicka, B.; Toliyat, H.A. A cycloidal magnetic gear with a novel flux shield ("moon") achieving higher torque density and lower unbalanced electromagnetic forces. *J. Magn. Magn. Mater.* **2023**, *571*, 170545. [CrossRef]
3. Ho, S.L.; Chau, K.T. An overview of magnetic gears. *Proc. IEEE* **2010**, *97*, 1999–2017.
4. Jian, L.; Chau, K.T.; Zhang, Z. Comparison of coaxial magnetic gears with different topologies. *J. Appl. Phys.* **2009**, *105*, 07F101.
5. Li, D.; Chau, K.T.; Liu, C. Optimization of coaxial magnetic gears using finite element analysis. *IEEE Trans. Magn.* **2012**, *48*, 4180–4183.
6. Rasmussen, P.O.; Andersen, T.O.; Jørgensen, F.T.; Nielsen, O. Development of a high-performance magnetic gear. *IEEE Trans. Ind. Appl.* **2011**, *41*, 764–770. [CrossRef]
7. Mabrouk, A.; Ksentini, O.; slim Abbes, M.; Haddar, M. Challenges and strategies in modeling and control of magnetic gears: A review. *J. Magn. Magn. Mater.* **2025**, *630*, 173412. [CrossRef]
8. Wang, Y.; Ho, S.L.; Fu, W.N. Multi-objective design of coaxial magnetic gears based on finite element analysis. *IEEE Trans. Magn.* **2016**, *52*, 1–4.
9. Ruoho, S.; Santa-Nokki, T.; Kolehmainen, J.; Arkkio, A. Modeling magnet length in 2-D finite-element analysis of electric machines. *IEEE Trans. Magn.* **2009**, *45*, 3114–3120. [CrossRef]
10. Zhu, Z.Q.; Lin, H.C.; Chen, J. Core loss and torque ripple analysis of coaxial magnetic gears. *IEEE Trans. Magn.* **2014**, *50*, 1–4.

11. Johnson, M.; Gardner, M.C.; Toliyat, H.A. A parameterized linear magnetic equivalent circuit for analysis and design of radial flux magnetic gears—Part I: Implementation. *IEEE Trans. Energy Convers.* **2017**, *33*, 784–791. [CrossRef]
12. Johnson, M.; Gardner, M.C.; Toliyat, H.A. A parameterized linear 3D magnetic equivalent circuit for analysis and design of radial flux magnetic gears—Part II: Evaluation. *IEEE Trans. Energy Convers.* **2021**, *36*, 2903–2911. [CrossRef]
13. Gerber, S.; Wang, R. Analysis of the end-effects in magnetic gears and magnetically geared machines. In Proceedings of the 2014 International Conference on Electrical Machines (ICEM), Berlin, Germany, 2–5 September 2014; IEEE: Piscataway, NJ, USA, 2014; pp. 396–402.
14. Gouda, E.; Mezani, S.; Baghli, L.; Rezzoug, A. Comparative study between mechanical and magnetic planetary gears. *IEEE Trans. Magn.* **2010**, *47*, 439–450. [CrossRef]
15. Wang, R.J.; Gerber, S. Magnetically geared wind generator technologies: Opportunities and challenges. *Appl. Energy* **2014**, *136*, 817–826. [CrossRef]
16. Scheidler, J.J.; Asnani, V.M.; Tallerico, T.F. NASA's magnetic gearing research for electrified aircraft propulsion. In Proceedings of the 2018 AIAA/IEEE Electric Aircraft Technologies Symposium (EATS), Cincinnati, OH, USA, 12–14 July 2018; IEEE: Piscataway, NJ, USA, 2018; pp. 1–12.
17. Galluzzi, R.; Circosta, S.; Amati, N.; Tonoli, A. Rotary regenerative shock absorbers for automotive suspensions. *Mechatronics* **2021**, *77*, 102580. [CrossRef]
18. Wong, H.Y.; Bird, J.Z.; Barnett, D.; Williams, W. A high torque density Halbach rotor coaxial magnetic gear. In Proceedings of the 2019 IEEE International Electric Machines & Drives Conference (IEMDC), San Diego, CA, USA, 12–15 May 2019; IEEE: Piscataway, NJ, USA, 2019; pp. 233–239.
19. Cameron, Z.A.; Tallerico, T.T.; Scheidler, J.J. Lessons learned in fabrication of a high-specific-torque concentric magnetic gear. In Proceedings of the Vertical Flight Society Annual Forum and Technology Display, Philadelphia, PA, USA, 13–16 May 2019; number GRC-E-DAA-TN67458.
20. Johnson, M.; Gardner, M.C.; Toliyat, H.A.; Englebretson, S.; Ouyang, W.; Tschida, C. Design, construction, and analysis of a large-scale inner stator radial flux magnetically geared generator for wave energy conversion. *IEEE Trans. Ind. Appl.* **2018**, *54*, 3305–3314. [CrossRef]
21. Li, K.; Modaresahmadi, S.; Williams, W.B.; Bird, J.Z.; Wright, J.D.; Barnett, D. Electromagnetic analysis and experimental testing of a flux focusing wind turbine magnetic gearbox. *IEEE Trans. Energy Convers.* **2019**, *34*, 1512–1521. [CrossRef]
22. Yan, B.; Li, X.; Wang, X.; Yang, Y. A review on the field-modulated magnetic gears: Development status, potential applications, and existent challenges. *IET Electr. Power Appl.* **2024**, *18*, 1–19. [CrossRef]
23. Montague, R.G.; Bingham, C.; Atallah, K. Magnetic gear pole-slip prevention using explicit model predictive control. *IEEE/ASME Trans. Mechatronics* **2012**, *18*, 1535–1543. [CrossRef]
24. Ferreira, C.; Vaidya, J. Torque analysis of permanent magnet coupling using 2D and 3D finite elements methods. *IEEE Trans. Magn.* **1989**, *25*, 3080–3082. [CrossRef]
25. Lee, J.; Chang, J. Analysis of the vibration characteristics of coaxial magnetic gear. *IEEE Trans. Magn.* **2017**, *53*, 1–4. [CrossRef]
26. Zanis, R.; Borisavljevic, A.; Jansen, J.; Lomonova, E. Modeling, design and experimental validation of a small-sized magnetic gear. In Proceedings of the 2013 International Conference on Electrical Machines and Systems (ICEMS), Busan, Republic of Korea, 26–29 October 2013; IEEE: Piscataway, NJ, USA, 2013; pp. 560–565.
27. Duan, G.; Gupta, T.; Sutton, E.; Wang, M.; Gardner, M.C.; Khan, S.A.; Praslicka, B. Cycloidal magnetic gear combining axial and radial topologies. *IEEE Trans. Energy Convers.* **2022**, *37*, 2130–2137. [CrossRef]
28. Kashani, S.A.A. Design and optimization of coaxial reluctance magnetic gear with different rotor topologies. *IEEE Trans. Ind. Electron.* **2021**, *69*, 101–109. [CrossRef]
29. Huang, Y.; Dong, J.; Zhu, J.; Guo, Y. Core loss modeling for permanent-magnet motor based on flux variation locus and finite-element method. *IEEE Trans. Magn.* **2012**, *48*, 1023–1026. [CrossRef]
30. Bertotti, G. General properties of power losses in soft ferromagnetic materials. *IEEE Trans. Magn.* **2002**, *24*, 621–630. [CrossRef]
31. Liu, G.; Liu, M.; Zhang, Y.; Wang, H.; Gerada, C. High-speed permanent magnet synchronous motor iron loss calculation method considering multiphysics factors. *IEEE Trans. Ind. Electron.* **2019**, *67*, 5360–5368. [CrossRef]
32. Steentjes, S.; Boehmer, S.; Hameyer, K. Permanent magnet eddy-current losses in 2-D FEM simulations of electrical machines. *IEEE Trans. Magn.* **2015**, *51*, 1–4. [CrossRef]
33. Saban, D.M.; Lipo, T.A. Hybrid Approach for Determining Eddy-Current Losses in High-Speed PM Rotors. In Proceedings of the 2007 IEEE International Electric Machines & Drives Conference, Antalya, Turkey, 3–5 May 2007; Volume 1, pp. 658–661.
34. Rens, J.; Vandenbossche, L.; Dorez, O. Iron Loss Modelling of Electrical Traction Motors for Improved Prediction of Higher Harmonic Losses. *World Electr. Veh. J.* **2020**, *11*, 24. [CrossRef]
35. Lee, S.H.; Im, S.Y.; Ryu, J.Y.; Lim, M.S. Optimum design process of coaxial magnetic gear using 3d performance prediction method considering axial flux leakage. *IEEE Trans. Ind. Appl.* **2023**, *60*, 3075–3085. [CrossRef]

36. Jing, L.B.; Luo, Z.H.; Liu, L.; Gao, Q.X. Optimization design of magnetic gear based on genetic algorithm toolbox of Matlab. *J. Electr. Eng. Technol.* **2016**, *11*, 1202–1209. [CrossRef]
37. Benesty, J.; Chen, J.; Huang, Y.; Cohen, I. Pearson correlation coefficient. In *Noise Reduction in Speech Processing*; Springer: Berlin/Heidelberg, Germany, 2009; pp. 1–4.
38. Praslicka, B.; Gardner, M.C.; Johnson, M.; Toliyat, H.A. Review and analysis of coaxial magnetic gear pole pair count selection effects. *IEEE J. Emerg. Sel. Top. Power Electron.* **2021**, *10*, 1813–1822. [CrossRef]
39. Matthee, A.; Wang, R.J.; Agenbach, C.J.; Els, D.N.; Kamper, M.J. Evaluation of a magnetic gear for air-cooled condenser applications. *IET Electr. Power Appl.* **2018**, *12*, 677–683. [CrossRef]
40. Kowol, M.; Kołodziej, J.; Gabor, R.; Łukaniszyn, M.; Jagieła, M. On-load characteristics of local and global forces in co-axial magnetic gear with reference to additively manufactured parts of modulator. *Energies* **2020**, *13*, 3169. [CrossRef]
41. Asnani, V.; Scheidler, J.; Tallerico, T.F. Magnetic gearing research at NASA. In Proceedings of the American Helicopter Society International Annual Forum & Technology Display, Phoenix, AZ, USA, 14–17 May 2018; number GRC-E-DAA-TN54810.
42. Wang, X.; Liu, D.; Lahaye, D.; Polinder, H.; Ferreira, J.A. Finite element analysis and experimental validation of eddy current losses in permanent magnet machines with fractional-slot concentrated windings. In Proceedings of the 2016 19th International Conference on Electrical Machines and Systems (ICEMS), Chiba, Japan, 13–16 November 2016; IEEE: Piscataway, NJ, USA, 2016; pp. 1–6.
43. Nair, S.S.; Wang, J.; Chen, L.; Chin, R.; Manolas, I.; Svechkarenko, D. Computationally efficient 3-D eddy current loss prediction in magnets of interior permanent magnet machines. *IEEE Trans. Magn.* **2016**, *52*, 1–10. [CrossRef]
44. Nair, S.S.; Wang, J.; Chen, L.; Chin, R.; Manolas, I.; Svechkarenko, D. Prediction of 3-D high-frequency eddy current loss in rotor magnets of SPM machines. *IEEE Trans. Magn.* **2016**, *52*, 1–10. [CrossRef]
45. Al-Timimy, A.; Al-Ani, M.; Degano, M.; Giangrande, P.; Gerada, C.; Galea, M. Influence of rotor endcaps on the electromagnetic performance of high-speed PM machine. *IET Electr. Power Appl.* **2018**, *12*, 1142–1149. [CrossRef]
46. Baninajar, H.; Modaresahmadi, S.; Wong, H.; Bird, J.; Williams, W.; Dechant, B. Experimental evaluation of a 63.3: 1 dual-stage coaxial magnetic gear. *IEEE Trans. Energy Convers.* **2022**, *38*, 158–169. [CrossRef]
47. Nair, S.S.; Wang, J.; Sun, T.; Chen, L.; Chin, R.; Beniakar, M.; Svechkarenko, D.; Manolas, I. Experimental validation of 3-D magnet eddy current loss prediction in surface-mounted permanent magnet machines. *IEEE Trans. Ind. Appl.* **2017**, *53*, 4380–4388. [CrossRef]
48. Nguyen, M.D.; Jung, W.S.; Hoang, D.T.; Kim, Y.J.; Shin, K.H.; Choi, J.Y. Fast Analysis and Optimization of a Magnetic Gear Based on Subdomain Modeling. *Mathematics* **2024**, *12*, 2922. [CrossRef]